

Upper crustal shear wave velocity and radial anisotropy beneath Jeju Island volcanoes from ambient noise tomography

Sang-Jun Lee¹, Seongryong Kim², Junkee Rhie³, Tae-Seob Kang⁴ and YoungHee Kim³

¹The Institute of Basic Science, Korea University, Seoul 02841, Republic of Korea

²Department of Earth and Environmental Sciences, Korea University, Seoul 02841, Republic of Korea. E-mail: seongryongkim@korea.ac.kr

³School of Earth and Environmental Sciences, Seoul National University, Seoul 8826, Republic of Korea

⁴Department of Earth and Environmental Sciences, Pukyong National University, Busan 48547, Republic of Korea

Accepted 2021 January 18. Received 2021 January 14; in original form 2020 November 17

SUMMARY

Jeju Island offshore of the southern Korean Peninsula is an isolated intraplate volcano formed by multiple basaltic eruptions from the Pleistocene (~ 1.8 Ma) to the Holocene (~ 3.7 ka). Due to the lack of available seismic data, magma structures at upper crustal depths of the island have not been clearly revealed. In this study, we imaged upper crustal isotropic and radial anisotropic structures beneath the island using ambient noise data from a temporary seismic network. A series of transdimensional hierarchical Bayesian inversions were performed to construct upper crustal (1–10 km) isotropic and anisotropic structures. Surface wave (Rayleigh and Love wave) group and phase velocity dispersion data were jointly inverted for 2–15 s. The results show that layers of negative anisotropy ($V_{\text{SH}} < V_{\text{SV}}$) are predominant at shallower (<2 km) and deeper (>5 km) depths, which was interpreted as reflecting dyke swarms responsible for the more than 400 cinder cones at the surface and the vertical plumbing systems supplying magma from deeper sources, respectively. Additionally, a layer with significantly positive radial anisotropy ($V_{\text{SH}} > V_{\text{SV}}$, up to 5 per cent) was found at middle depths (2–5 km), and was interpreted as horizontally aligned magma plumbing systems (e.g. sills) through comparisons with several other volcanoes worldwide. In comparison with the isotropic structure, the positive anisotropic layer was separated into upper and lower layers with locally neutral to slightly fast and slower shear wave velocities, respectively, beneath the largest central crater (Mt Halla). Such a structure indicates that the cooled upper part of the magma plumbing systems formed within the horizontally developed sill complex, and is underlain by still-warm sill structures, potentially with a small fraction of melting. With dykes predominant above and below, the island-wide sill layer and locally high-temperature body at the centre explain the evolution of the Jeju Island volcanoes by island-forming surface lava flows and central volcanic eruptions before and after the eruptions of cinder cones.

Key words: Tomography; Seismic anisotropy; Seismic noise; Surface waves and free oscillation; Crustal structure.

1 INTRODUCTION

Knowledge of the magma plumbing system in the shallow crust is important for understanding the evolution of volcanoes at the surface (Brenquier *et al.* 2007; Huang *et al.* 2015; Spica *et al.* 2015, 2017; Li *et al.* 2016). Though ideally simple vertical dyke systems have been assumed in many studies, recent higher-resolution studies using seismic, geological and geodetic data have shown that the various types of magma structures, including dykes, chambers and sills, interact with each other in the formation of volcanoes (Klügel

et al. 2005; Ishizuka *et al.* 2008; Peltier *et al.* 2009; Paulatto *et al.* 2010; Chadwick *et al.* 2011; Bagnardi & Amelung 2012; González *et al.* 2013; Jaxybulatov *et al.* 2014; Huang *et al.* 2015; Mordret *et al.* 2015; Tibaldi 2015). It has been suggested that the development of complex magma plumbing systems is affected by the local stress field or inherent structures (e.g. topography, fault, collapsed caldera structure, etc.), not simply by tectonic regimes related to the motion of neighbouring plates (Ishizuka *et al.* 2008; Tibaldi 2015; González *et al.* 2013). Therefore, more comprehensive and detailed analysis is required to better understand the development of volcanic systems.

Many seismic studies have been conducted to detect magma structures in the crust using local traveltome tomography and ambient noise tomography (Aloisi *et al.* 2002; Brenguier *et al.* 2007; Stankiewicz *et al.* 2010; Huang *et al.* 2015), primarily by identifying velocity anomalies. These approaches may be more effective for obtaining high-resolution images by accumulating many data points from dense temporary and permanent seismic stations (Jaxybulatov *et al.* 2014; Mordret *et al.* 2015; Benediktsdóttir *et al.* 2017; Godfrey *et al.* 2017; Judd *et al.* 2017; Jiang *et al.* 2018; Lynner *et al.* 2018). Another important property that is used to identify magma structures is seismic anisotropy, which is particularly useful to detect alignment or layering of magma structures beneath volcanoes (Xie *et al.* 2013; Jaxybulatov *et al.* 2014; Mordret *et al.* 2015; Lynner *et al.* 2018). Therefore, studies into which both isotropic and anisotropic structures are incorporated, especially using data from many stations, provide unique opportunities to validate each other and to identify more detailed and specific processes in the development of volcanoes. The isotropic and radially anisotropic structures were routinely estimated using Rayleigh and Love wave dispersion data from ambient noise (Jaxybulatov *et al.* 2014; Mordret *et al.* 2015; Judd *et al.* 2017; Lynner *et al.* 2018).

Jeju Island (JI) comprises intraplate volcanoes within a relatively small area (2400 km^2) located in the southwest offshore of the Korean Peninsula; it is separated by more than 600 km from the southern (and nearest) subduction zone. There has been no evidence of current volcanic activity on or proximal to JI, and the nearest intraplate volcano is 200-km away (Tatsumi *et al.* 2004; Brenna *et al.* 2012; Koh *et al.* 2013; Yoon *et al.* 2014; Brenna *et al.* 2015, Fig. 1). Since there is a lack of volcanic activity and no seismicity, volcanic structures have not been well studied seismically. Though there have been some regional studies, including JI (e.g. Zheng *et al.* 2011; Kim *et al.* 2016), it is difficult to identify magma structures beneath its volcanoes.

Recently, Song *et al.* (2018) presented teleseismic tomography results using data from a temporary seismic network installed on JI, which suggested the existence of a complex, lithosphere-scale magma structure in which sublithospheric magma interacts with the lithosphere along multiple, laterally spreading paths. Moreover, they suggested the existence of a relatively thicker continental lithosphere in the north and west of JI that could cause decompression melting via localized mantle convection. This model would explain the isolated occurrence of volcanism on JI, far from subduction zones and other intraplate volcanoes, and shows that JI was formed by multistep eruptions of magma of varied durations, spatial extents and compositions. Taking into account the methods and data of Song *et al.* (2018), the shallow crust of JI cannot be estimated due to the lack of resolution, which is critical to fully explaining how magma is supplied to and distributed among surface volcanoes, as well as how the central crater formed near the surface. In this study, we aimed to estimate shallower ($\sim 5 \text{ km}$) magma plumbing structures beneath volcanoes on JI using data from the same stations as reported by Song *et al.* (2018).

In this study, we constructed isotropic and anisotropic shear wave velocity models for the shallow crust ($< 10 \text{ km}$) of JI using ambient noise tomography from the continuous recordings of 20 temporary and three permanent stations deployed over 3 yr. To investigate volcanoes without current seismic activity, ambient noise tomography using dense temporal network data was found to be a suitable approach. In particular, magma structures at various depths, including in the shallow crust, may be effectively estimated using this method, depending upon the size of the seismic array (Jaxybulatov *et al.* 2014; Mordret *et al.* 2015; Kim *et al.* 2017; Jiang *et al.* 2018).

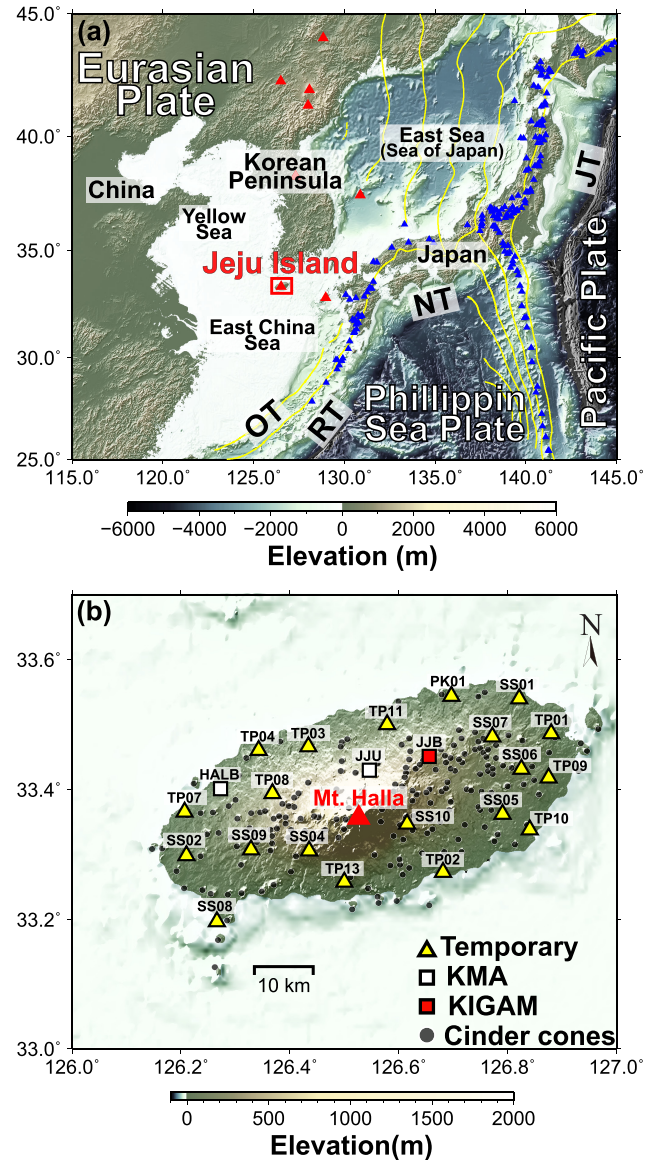


Figure 1. (a) Location and topographic map of Jeju Island (JI) and the surrounding region. The yellow contour indicates the subduction depth of the Pacific Plate and Philippine Sea Plate. (b) Distribution of seismic stations and cinder cones (dark grey circles) on JI (after Song *et al.* 2018). Portable (yellow triangles) and permanent (white and red rectangles) broad-band seismic stations are evenly distributed across the island. OT, Okinawa Trough; RT, Ryukyu Trench; NT, Nankai Trough; JT, Japan Trench. Red triangles indicate intraplate volcanoes, and blue triangles indicate arc-volcanoes.

We measured the fundamental mode of surface wave (Rayleigh and Love waves) group and phase velocity dispersion curves using three-component continuous data. To better constrain anisotropic parameters, a recently developed transdimensional and hierarchical Bayesian technique was used for joint inversion, which uses Rayleigh and Love wave data and estimates isotropic and anisotropic structures simultaneously. Through these analyses, we were able to generate 3-D seismic images that reveal the magma plumbing system in the shallow crust beneath JI for the first time.

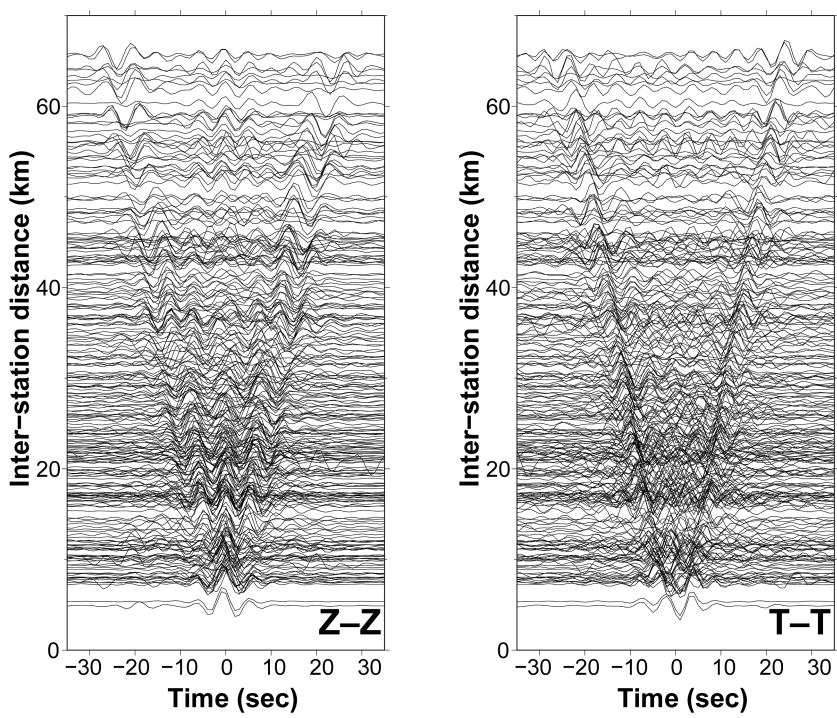


Figure 2. Calculated cross-correlation sections for (a) Z–Z and (b) T–T component pairs. A 5–15-s bandpass filter was applied.

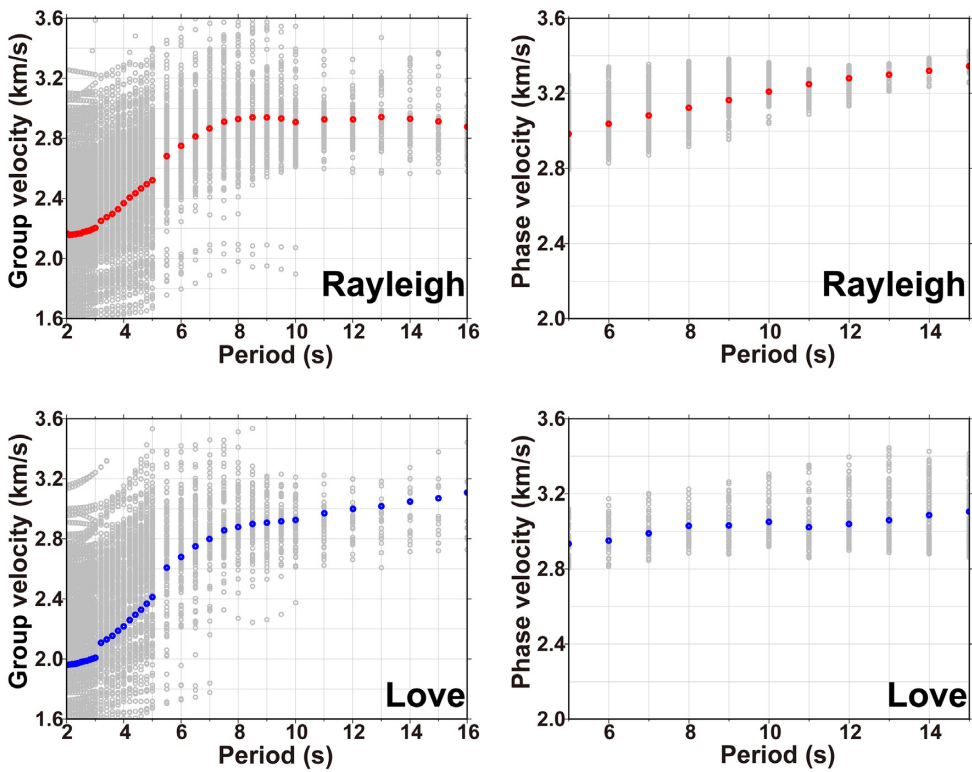


Figure 3. Group and phase velocity dispersions of Rayleigh and Love waves extracted from cross-correlations using the multifilter technique of Herrmann & Ammon (2002). Red and blue dots represent the mean of the measured dispersion data.

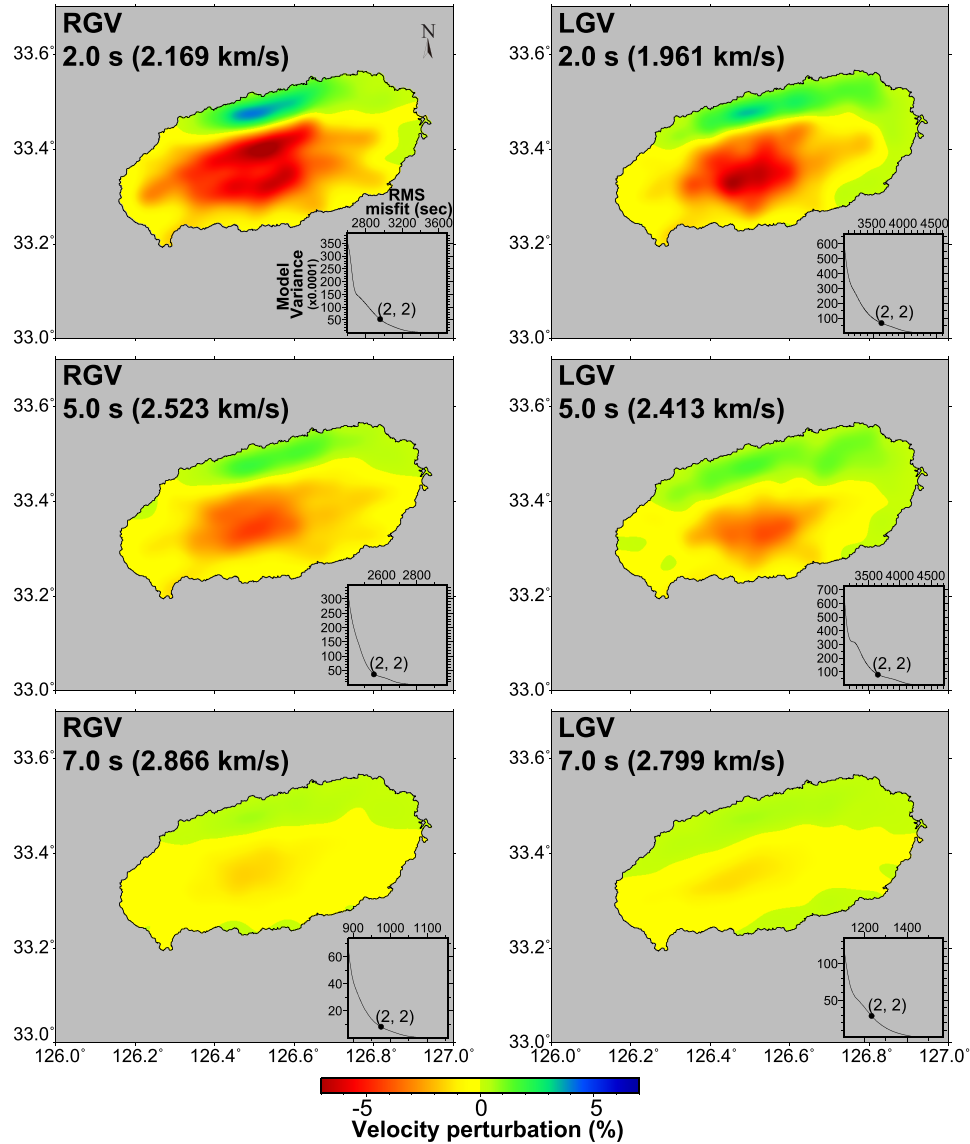


Figure 4. Examples of constructed Rayleigh wave group velocity (RGV) and Love wave group velocity (LGV) maps of JI for 2, 3 and 7 s. The trade-off curve and selected smoothing and damping parameters are also plotted in the lower right-hand corner of each velocity map.

2 GEOLOGICAL SETTING AND BACKGROUND

2.1 Geological history and previous studies

Similar to other intraplate volcanoes distributed around the Korean Peninsula, JI has existed in an isolated location without neighbouring volcanoes since its formation during the early Pleistocene (~ 1.7 Ma). Until the recent crater-forming eruption at the centre of JI (~ 3.7 ka), JI suffered four stages of eruptions with variable magma compositions, from the alkali to tholeiitic basalts (Tatsumi *et al.* 2004; Brenna *et al.* 2012, 2015; Koh *et al.* 2013; Yoon *et al.* 2014). As a result, the largest volcano (Mt Halla) was created at the centre of the island with ~ 400 monogenic cinder cones distributed across JI (Park *et al.* 2008; Shin *et al.* 2012; Koh *et al.* 2013; Brenna *et al.* 2015).

Previous studies on the formation of JI volcanoes have mainly focused on the magma source and timing of eruptions based on the geochemical properties of volcanic rocks, which indicated that the magma originated either from interactions between a shallow mantle and a deep plume (Nakamura *et al.* 1990; Tatsumi *et al.* 2004) or from the sublithospheric upper mantle (Kim *et al.* 2019) with separate paths (Brenna *et al.* 2012, 2015). Additionally, Shin *et al.* (2012) interpreted the magnetic anomaly around JI and proposed that lithospheric folding beneath the island could generate basaltic magma, while Choi *et al.* (2001) proposed substantial interactions with the lithospheric structure of the magma from xenolith data.

Seismologically, the magmatic structures in the crust of JI have not been well-sampled. A shallow (< 2 km) 1-D crustal shear wave velocity structure was initially studied using the spatial autocorrelation (SPAC) method (Kim & Hong 2012). The crustal thickness beneath JI was estimated from the inversion of receiver functions

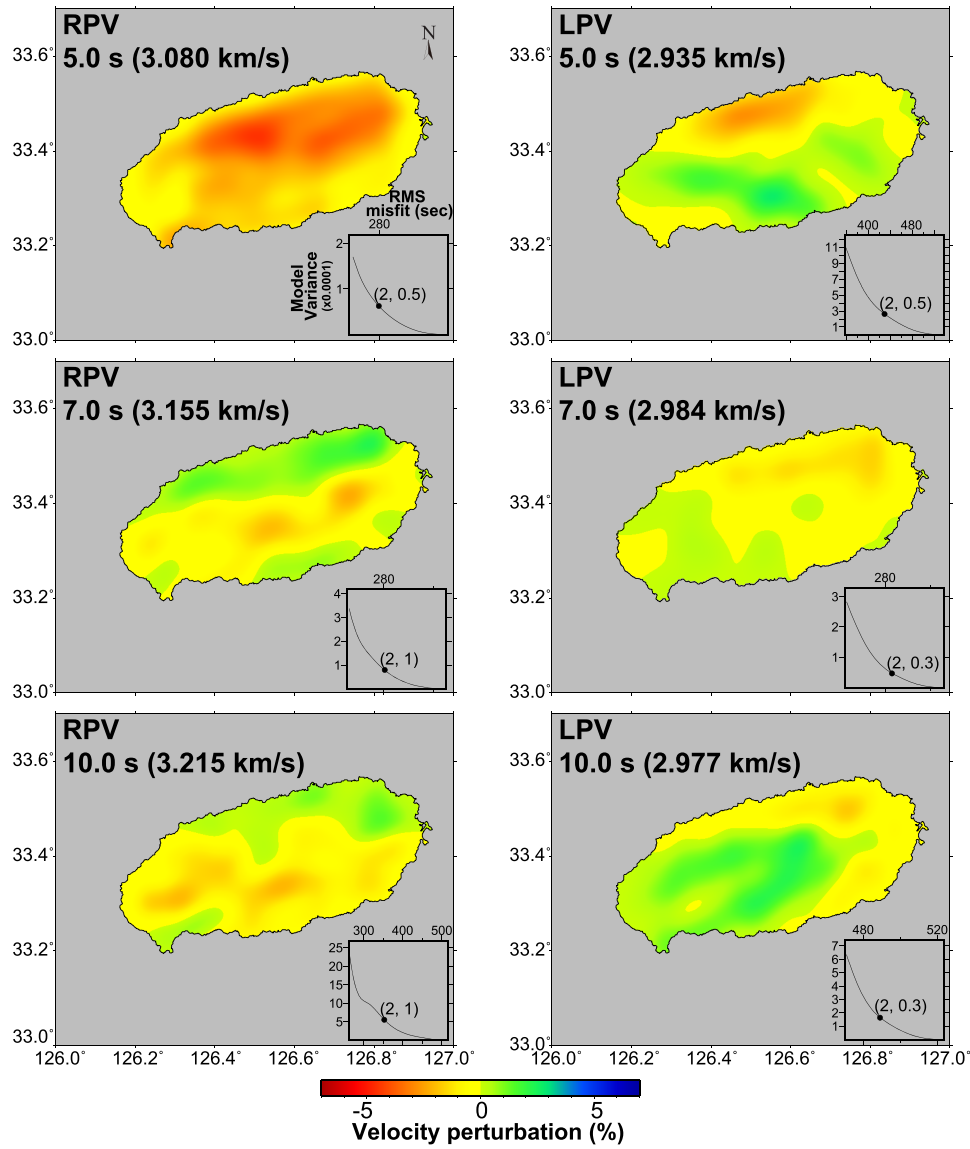


Figure 5. Examples of constructed Rayleigh and Love phase velocity (RPV and LPV, respectively) maps of JI for 5, 7 and 10 s. The trade-off curve and selected smoothing and damping parameters are also plotted in the lower right-hand corner of each velocity map.

using data from permanent seismic stations on the island (Jeon *et al.* 2013). However, these studies were conducted over limited areas of JI due to the lack of available data.

2.2 Radial anisotropy in the volcanic field

Anisotropy observed in the crust is generally explained by a shape-preferred orientation (SPO) or crystallographic-preferred orientation (CPO). The former is generally caused by structures aligned to a specific direction (e.g. crack, fault, melt lenses, etc.), while the latter is related to mineral alignments due to sedimentation and deformation (Crampin 1981, 1984, 1989; Shapiro *et al.* 2004; Meissner *et al.* 2006; Eilon *et al.* 2014; Ko & Jung 2015; Almqvist & Mainprice 2017; Jung 2017; Kim & Jung 2019; Russell *et al.* 2019).

For volcanic structures, the radial anisotropy of shear wave velocities is used to identify magma-related structures (Mainprice & Nicolas 1989; Leary *et al.* 1990; Crampin & Lovell 1991; Shapiro *et al.* 2004; Meissner *et al.* 2006). The origin of these structures and mineral alignments determine the orientation of the fast shear wave velocity (V_{SH} or V_{SV}) axes (Mordret *et al.* 2015; Spica *et al.* 2017). Positive radial anisotropy ($V_{SH} > V_{SV}$) primarily originates from either horizontally intruded structures (e.g. sill or melt lenses), frozen lava flows or pyroclastic deposits. However, negative radial anisotropy ($V_{SV} > V_{SH}$) is the result of vertically oriented intrusions (e.g. dykes) and cracks. An effective way to measure radial anisotropy is through the comparison of Rayleigh (for V_{SV}) and Love (for V_{SH}) waves, particularly from ambient noise data (Huang *et al.* 2010; Moschetti *et al.* 2010; Guo *et al.* 2012, 2016). Consequently, measured radial anisotropy provides answers to questions related to the magma plumbing system, including how magma was supplied,

what predominant direction of magma intrusion was, and whether or not shallow chambers exist (Mordret *et al.* 2015; Benediktsdóttir *et al.* 2017; Godfrey *et al.* 2017; Judd *et al.* 2017; Lynner *et al.* 2018).

3 DATA AND METHODS

3.1 Data

A comprehensive three-component broad-band data set was used from 20 temporary and 3 permanent seismic stations. The three permanent stations were equipped with three-component broad-band sensors. The temporary network was jointly operated by Seoul National University and Pukyong National University (Fig. 1). The 20 instruments that were used at the temporary stations consist of Nanometrics Trillium compact broad-band sensors with Taurus digitizers (Nanometrics Inc., Canada). Three temporary pilot stations were installed in advance from March 2013. Thereafter, additional 17 stations were deployed over JI from September 2013 to February 2017. The locations of the pre-existing permanent stations (i.e. HALB, JJU and JJB) were taken into account when the temporary stations were deployed, to design a more evenly distributed network. The temporary stations were located on relatively flat basaltic lava fields, except for five stations. Three of the stations that were located in the east (SS05, SS06 and SS07) were at the cinder cone tops and two (SS04 and SS10) were installed on the Mt Halla slope. The altitude of the highest station was ~ 700 m, whereas the lowest station was located near sea level. This study analysed 2-yr-long continuous three-component data from January 2014 to December 2015 when the continuous data from all of the stations (20 temporary and 3 permanent stations) were fully available.

3.2 Data processing and estimation of surface dispersion maps

We used well-established ambient noise cross-correlation methods to process our data and obtain surface wave dispersion curves (e.g. Bensen *et al.* 2007; Lin *et al.* 2008). Instrument response, mean values, and trends were removed from the three-component continuous waveforms, and divided by 1-hr-long time windows. Afterward, the windowed data were decimated to 1 Hz and band-pass filtered between 0.01 and 0.45 Hz. We applied one-bit time domain normalization and spectral whitening in the frequency domain. Lastly, cross-correlation functions were calculated for all available station-pairs and stacked. The horizontal component cross-correlations (i.e. east–east, E–E; east–north, E–N; north–east, N–E and north–north, N–N) are commutative with the rotation operator. Therefore, the transverse–transverse (T–T) cross-correlations between each station-pair can be extracted using a linear combination of the horizontal component cross-correlations with coefficients that are related to the interstation azimuth and backazimuth angles (Lin *et al.* 2008). Finally, 253 cross-correlograms were calculated for both vertical–vertical (Z–Z) and transverse–transverse (T–T) components. Thereafter, 224 and 223 correlograms were selected for Z–Z and T–T, which showed that there were clear signals of Rayleigh and Love waves, respectively (Fig. 2).

To estimate group and phase velocities from the fundamental modes of Rayleigh and Love waves, a multifilter analysis (e.g. Herrmann & Ammon 2002; Yao *et al.* 2006) was applied to the obtained cross-correlograms. We automatically measured group and phase velocities using an iterative process. During the initial iteration,

preliminary dispersion curves were estimated based on a reference curve calculated from a 1-D velocity model of the Korean Peninsula (Kim *et al.* 2011). Then, the mean of the previously measured dispersion curves of all station-pairs was used as a reference dispersion curve for the next time measurements. This process was repeated for additional three times to calculate the final dispersion curves for the group and phase velocities (Fig. 3).

Spatial distributions of group and phase velocities in different wave periods were estimated using a non-linear 2-D tomographic method, which combined a fast marching method and subspace inversion (Kennett *et al.* 1988; Rawlinson & Sambridge 2005). Therefore, 2-D group and phase velocity maps of the Rayleigh and Love waves were constructed within 2–15 s and 5–15 s for the group and phase velocities, respectively (Figs 4 and 5). To account for the trade-offs between data misfit and model variance, we determined optimum sets of damping and smoothing values by selecting elbow-points in L-curve analyses (insets in Figs 4 and 5).

3.3 Construction of a 3-D model from Bayesian joint inversions

The 3-D isotropic and anisotropic velocity structures were estimated by performing a series of 1-D inversions for 461 nodes over a geographical grid spacing of 0.02° . Four dispersion data were composed for each gridpoint through interpolation using dispersion velocity maps, within 2–16 s and 5–15 s for the group and phase velocities, respectively (Figs 4 and 5). The Bayesian inversion technique established by Kim *et al.* (2017) was used for 1-D inversions. This approach offered several specific advantages when applied to the data in this study. First, the inversion parameter values were estimated using a fully non-linear Markov chain Monte Carlo (MCMC) sampling without assuming arbitrary constraints (e.g. initial models). Therefore, the full probability density distributions for inversion parameters (i.e. posterior probability distribution or PPD) could be obtained, which allowed for the estimation of the resulting model uncertainties. The MCMC sampling of probability densities enabled the implementation of simultaneous searches for multiple parameters (e.g. isotropic and radially anisotropic velocities) in a layer to be straightforward during the inversion process. Secondly, the inversion technique of Kim *et al.* (2017) with the hierarchical scheme in the method allows different weightings to be automatically imposed by searching for different noise levels in different types of data that are based on the information within the data. The noise level in these data types is a critical factor when determining the goodness of fit between the proposed model and the measured data. This is particularly useful for obtaining less biased results in joint inversions when using several different types of data, where arbitrarily selected data weightings are often selected for conventional joint inversions. Finally, the transdimensional scheme in the inversion process searches a set of optimum parameters (i.e. numbers of layers) to balance the trade-offs between model roughness and data misfit. This study used reasonably broad and flat distributions for the prior probabilities (or search ranges) of the inversion parameters. These include isotropic V_S ($V_{ISO} = 0.5\text{--}5.0 \text{ km s}^{-1}$), V_P/V_S ratio that is equal to 1.5–2.0, radial anisotropy ($\xi = -50$ to 50 per cent), interface depths (0–40 km), the number of layers (2–30) and the scaling factors for noise levels (−5.0 to 5.0). Consequently, no damping or smoothing is required when using this technique. The isotropic velocity was defined as $V_{ISO} = (2V_{SV} + V_{SH})/3$ and radial anisotropy as $\xi = 100 \times (V_{SH} - V_{ISO})/V_{ISO}$ (Jiang *et al.* 2018; Lynner *et al.* 2018). This study adopted the method for 1-D inversions of

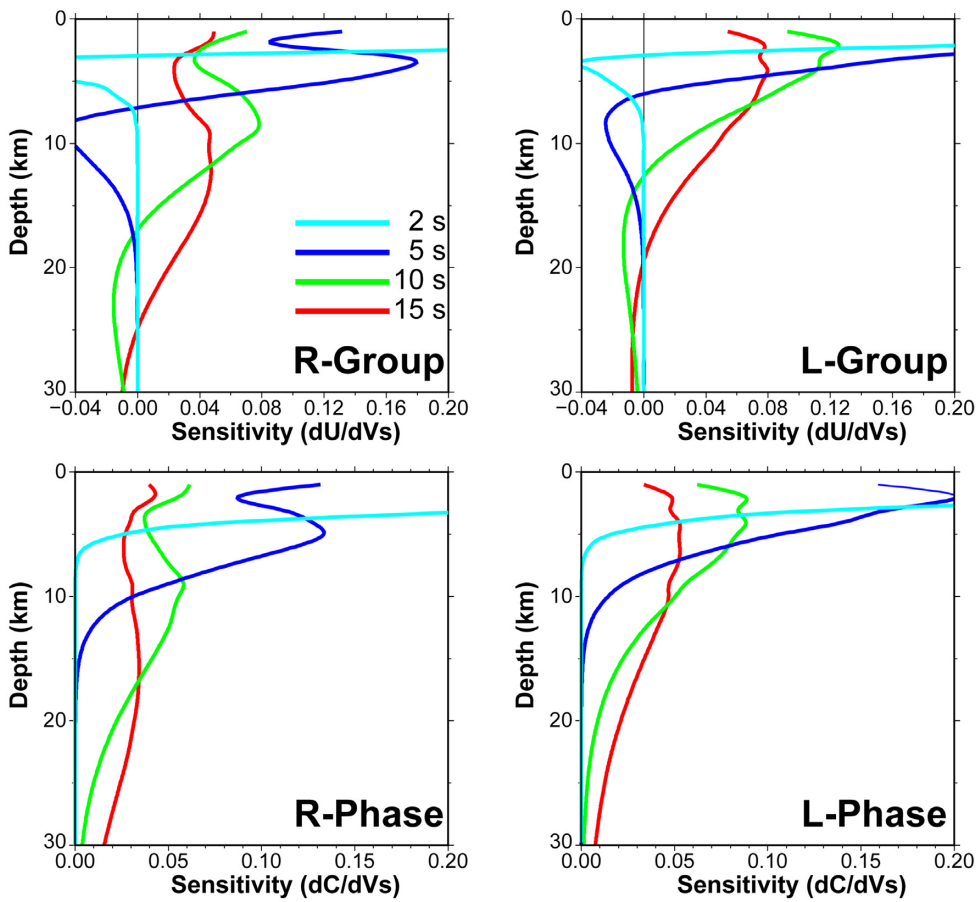


Figure 6. Sensitivity kernel at 2, 5 and 15 s using the 1-D average model of JI from the study of Kim *et al.* (2016b). The Rayleigh and Love wave group/phase velocities for periods of 2 and 15 s are sensitive to shear wave velocities at depths of up to 15 km.

461 gridpoints with four different types of surface dispersion data, which consisted of Rayleigh and Love wave group and phase velocity dispersions. The Markov chain was run for 50 000 iterations for each inversion. Furthermore, the first half was discarded to obtain converged samples from the latter half.

4 RESULTS

4.1 Dispersion velocity maps

In Rayleigh wave group velocity (RGV) maps (Fig. 4), a low velocity anomaly was consistently observed in the centre of JI, with a maximum amplitude of ~7 per cent in the short period maps (2–3-s period) and weaker for longer periods. Along the northern part of JI, a high-velocity anomaly was found with a perturbation of up to 4 per cent faster than the average of each period. The pattern of velocity perturbations was maintained in the Love wave group velocity (LGV) maps (Fig. 4), which had slightly weaker amplitudes (6 and ~3 per cent average values for fast and slow anomalies, respectively) than the RGV maps. For the RPV and RGV maps, the velocity anomalies were weaker than those of the group velocity maps (Fig. 5). Calculated sensitivity kernels (Fig. 6) showed that phase velocity data sampled deeper depths than group velocity data for the same wave period and provided more reliable estimates to at least 10 km, given the ranges of data periods used in our inversions (Fig. 6).

In order to evaluate the lateral resolution of the velocity maps (Figs 4 and 5), we performed a series of checkerboard tests with velocity perturbations of ± 5 per cent in $0.08^\circ \times 0.08^\circ$ checkers. The results (Fig. 7) showed that the input anomalies were generally well recovered, particularly for 5 s RGV and LGV maps, and 10 s RPV maps (Fig. 7). Since the velocity anomalies of the velocity maps were larger than $0.08^\circ \times 0.08^\circ$, it could be confirmed that the anomalies were undistorted, even considering the path coverage. However, the LPV result was distorted in the northeast–southwest direction over a 10 s period. This is due to the shape of the temporary network, which is installed along an elliptical shape across JI, and a smaller number of cross-correlograms used for LPV (~ 120) than for the RGV, LGV and RPV maps (generally > 200).

4.2 1-D Bayesian inversions

Fig. 8 shows an example of the 1-D inversion results for a gridpoint at the central volcano (Mt Halla, 33.36°N , 126.52°E). The marginal PPDs of V_{ISO} and ξ show sharp changes at ~ 2 and ~ 5 km depths in a general trend wherein the velocity increases with depth (Fig. 8a). The marginal distribution of layer boundaries (Fig. 8a) confirms that higher probabilities were found at the corresponding depths. Though the PPDs provide credible ranges, we focus on the depth range of 1–10 km based on the calculated sensitivity kernels (Fig. 6) and resolution of the dispersion maps (Fig. 7).

It was noted that the depth sensitivity of the data was reasonably high at depths greater than 10 km; therefore, the interpreted

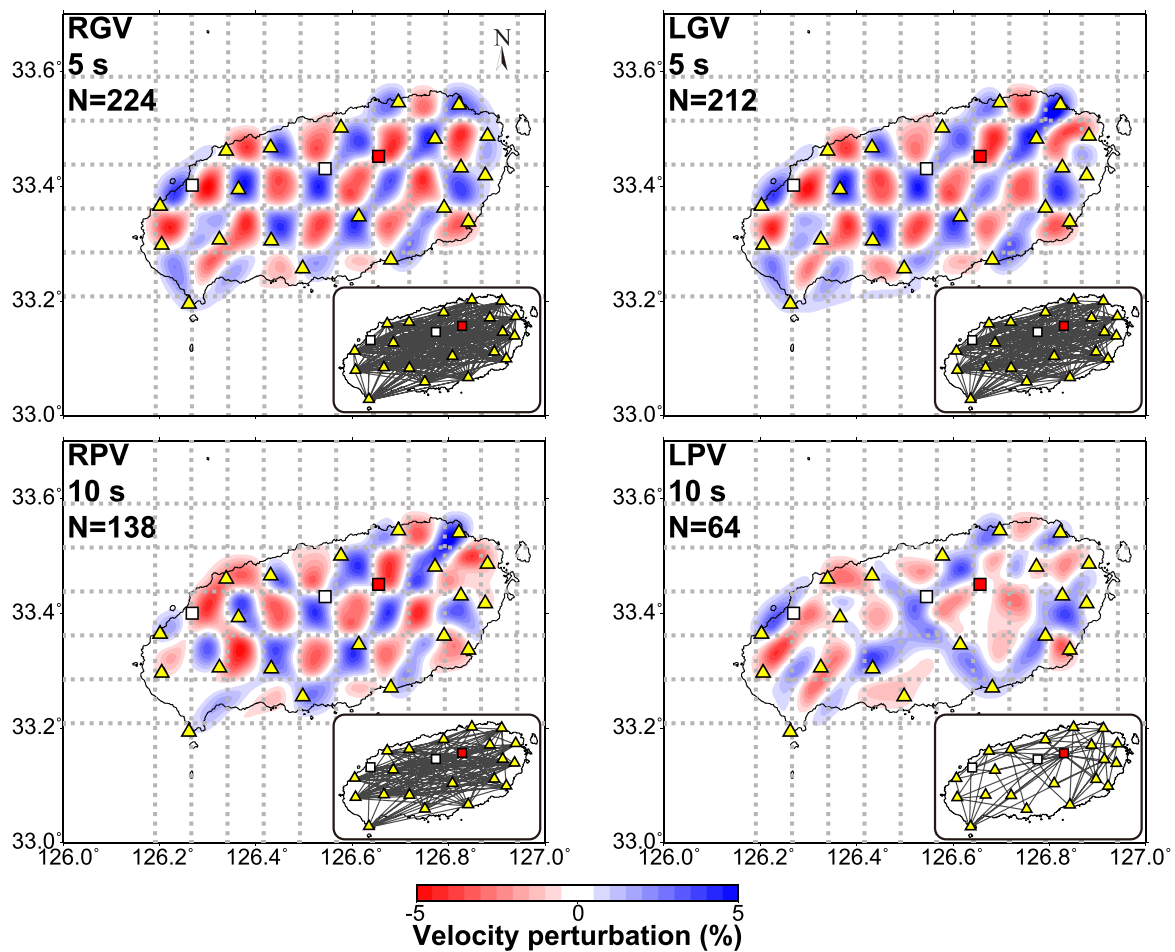


Figure 7. Checkerboard test results for RGV and LGV at 5 s and RPV and LPV at 10 s. A grid size of $0.08^\circ \times 0.08^\circ$ (grey dashed line) was used in the calculations. In each map, the number of used ray paths (N) is shown on the top left-hand side and the distribution of ray paths is presented in the inset.

depth range was a conservative choice to present the most reliable shallow magma structures. An interesting trend in most of inversion results was the layering of different anisotropic structures (e.g. Bodin *et al.* 2016) through a combination of strong negative radial anisotropy ($V_{SV} > V_{SH}$) at depths < 2 km, strong positive radial anisotropy ($V_{SH} > V_{SV}$) from 2 to 5 km and another negative value at depths > 5 km. This pattern is reliable when the $\pm 2\sigma$ ranges of the marginal PPD for ξ are taken into account.

The marginal PPD for the number of layers (Fig. 8b) revealed that the inversion results comprised many different models with different numbers of layers, which fit both the Rayleigh and Love wave dispersion data (Fig. 8c). A test inversion assuming isotropic structures using the same data (Fig. 9) resulted in a similar marginal distribution of isotropic shear wave velocity models and a good fit to RGV and RPV. However, the constrained inversion exhibited a poorer fit to LGV and LPV (Fig. 9c) than those in Fig. 8(c) at shorter and longer periods in LGV and longer periods in LPV, which correspond to the highly anisotropic layers shown in Fig. 8(a). An F -test was performed to evaluate if the increase in the number of parameters made a significant improvement in fitting the observed data with synthetic data (Song *et al.* 2004; Tomar *et al.* 2017). Statistical parameter F_{cal} , which shows the degree of improvement in the anisotropic inversion over the isotropic inversion, is significantly larger than $F_{0.95}$ ($F_{cal}: 123.1$; $F_{0.95}: 10.86$) which represents a 5 per cent rejection level for the residual estimate sum. Therefore, the

anisotropic inversion result is statistically superior to that of the isotropic inversion.

4.3 Isotropic and anisotropic 3-D models

We constructed isotropic and radially anisotropic 3-D velocity structure models by integrating the results of the 1-D Bayesian inversions individually performed at 461 grid nodes (Figs 10 and 11). In the V_{ISO} model (Fig. 10), a broad, low-velocity anomaly (lower than -8 per cent) was found at 1.5 km beneath the central area in JI, including the Mt Halla volcano (L_V1 in Fig. 11). Meanwhile, the northern coast exhibited a relatively high velocity anomaly (~ 3 per cent). The pattern changed significantly from 2 km, where all of JI exhibits normal velocities, with slightly higher (~ 2 per cent) velocities around the central region (L_V2). At depth of ~ 4 km, low-velocity anomalies (lower than -4 km s^{-1}) were found within a limited area beneath the central volcano (L_V3). From depths greater than 5 km (L_V4), the variation in velocity was small, with a range from 1 to -2 per cent to the mean value in this region (~ 3.48 km s^{-1}), which is slower than the mean upper-middle crustal velocity (~ 3.6 km s^{-1}) in the southern Korean Peninsula (Kim *et al.* 2011) and corresponds to the results from teleseismic tomography using body wave data in this region (Song *et al.* 2018).

In the radial anisotropy model (Fig. 10), strong negative radial anisotropy ($\xi < -12.5$ per cent) was observed at shallow depths

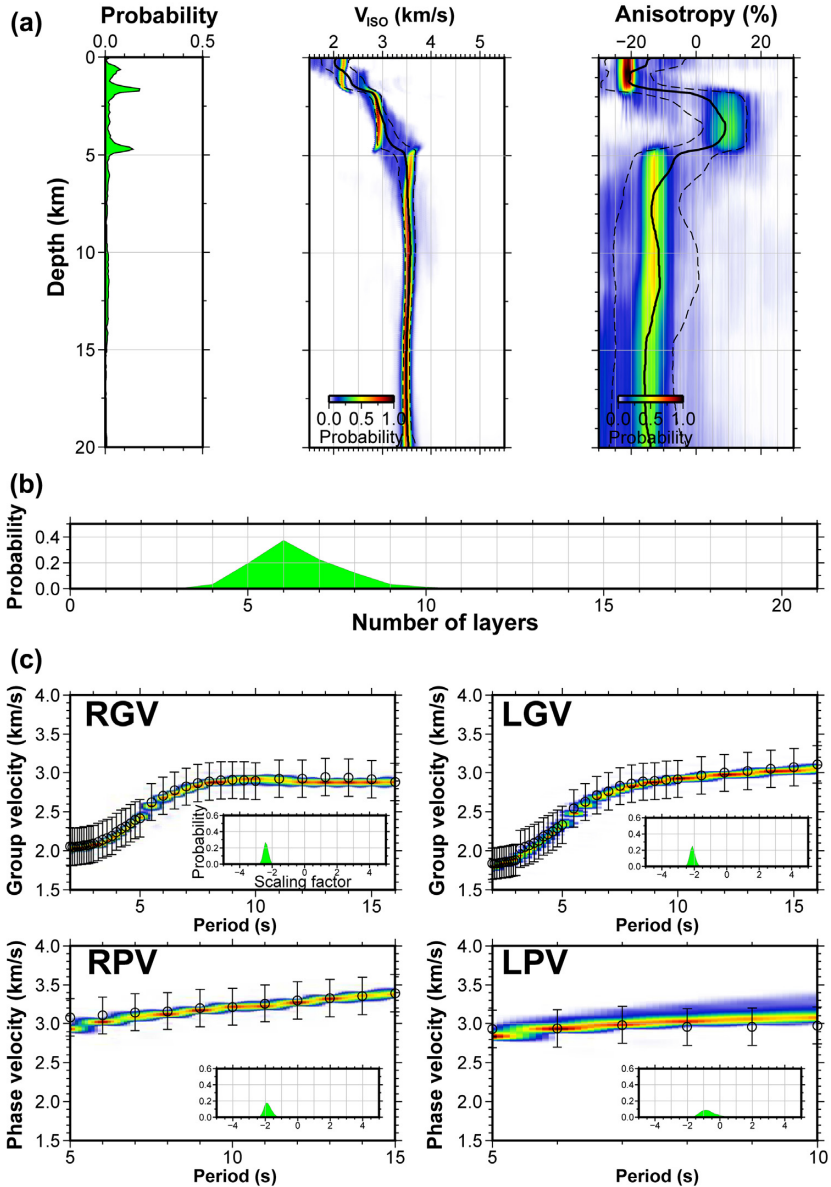


Figure 8. An example of a 1-D shear velocity model with results of the Bayesian inversion using Rayleigh and Love wave dispersions at 33.36°N , 126.52°E . Posterior probability distribution (PPD) of (a) layer boundaries, shear wave velocity, density, and anisotropy with depth, (b) the number of layers, and (c) the predicted synthetic and observed data with error bars. A total of four different types of dispersion data for Rayleigh and Love wave group velocities (period: 2–15 s) and Rayleigh and Love wave phase velocities from this study (period: 5–15 s) were jointly inverted using a hierarchical and transdimensional Bayesian technique.

(<2 km) beneath the entire JI region (L_{A1} in Fig. 11). In the same area but at deeper depths (>5 km), slightly weaker negative anisotropy ($<\sim 7.5$ per cent, L_{A3}) was observed. In contrast, positive anisotropic structures were included at the depth range between 2 and 5 km (L_{A2}). The horizontally fast structure was the thickest beneath the central volcano, with a thickness of 3 km, and the anisotropic structure thinned to 1.5 km towards the outside of JI. The thicker part corresponds to the region with large perturbations of isotropic velocities beneath the central volcano. Fig. 11 shows vertical profiles of the V_{ISO} and ξ models along the long axis (A–A') and the short axis (B–B') of the ovoid JI (Fig. 10). By combining the patterns described in the V_{ISO} and ξ models, upper crustal structures beneath JI were identified and categorized into a structure with three layers over a basement, including:

- (1) A top layer down to 2 km with slow V_{ISO} (lower than -8 per cent, L_{V1}) and strongly negative ξ (less than -12.5 per cent, L_{A1}).
- (2) A second layer with positive ξ (>5 per cent, central top of L_{A2}) and slightly fast V_{ISO} (2–4 per cent, L_{V2}) at depths between 2 and 3 km, particularly beneath the central volcano and within areas of ~ 20 and ~ 10 km along the major and minor axes of JI, respectively.
- (3) A third layer with the same magnitude of positive ξ (L_{A2}) and relatively slow V_{ISO} (lower than -4 per cent, L_{V3}) in a similar area to the upper layer, but at depths between 3 and 5 km.
- (4) A vertically fast basement ($\xi > 7.5$ per cent, L_{A3}) with generally neutral V_{ISO} over across JI (L_{V4}).

It is notable that the pattern changes moving away from the centre of JI. The structure with the first positive ξ becomes thinner, and

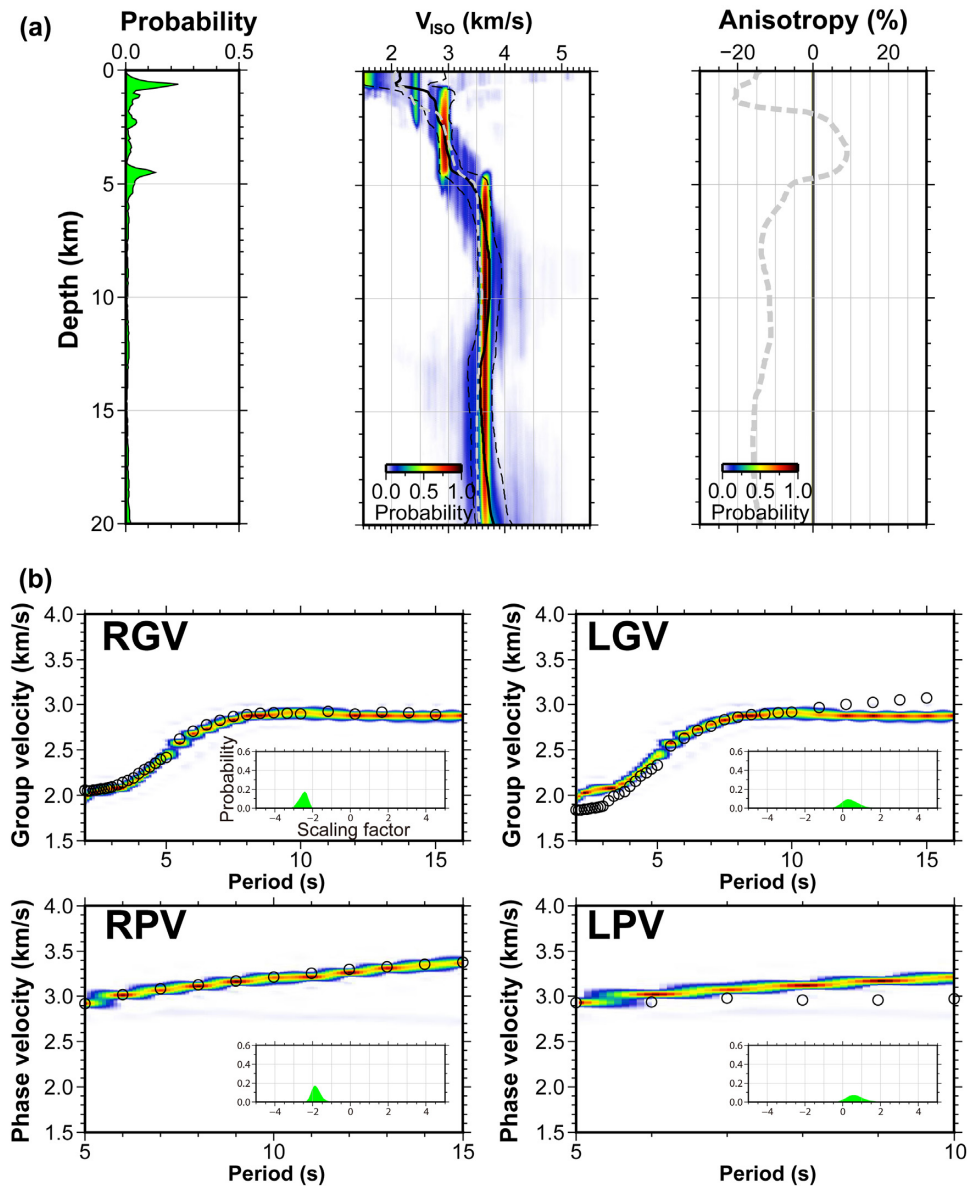


Figure 9. The same results as those shown in Fig. 8, less the number of layers (Fig. 8b), but with isotropic inversion applied. Grey dashed lines represent the anisotropic inversion results shown in Fig. 8.

thus is located at the depth corresponding to the third layer (3–5 km, L_V3), with more neutral isotropic velocities at all depth ranges except for the top layer.

5 DISCUSSION

JII exhibits significant topographic variation from sea level to 1.95 km at the top of Mt Halla, all within a limited ovoid area of approximately 75 km × 32 km. In this study, we assumed a flat surface to estimate the distribution maps of surface wave dispersion velocities and the final 3-D models, similarly to the assumptions made in previous studies (Jaxybulatov *et al.* 2014; Benediktsdóttir *et al.* 2017; Jeddi *et al.* 2017). This is due to the fact that the propagation of surface waves along uneven surfaces is complex, difficult

to understand and dependent upon wave periods, in contrast to studies using the rays of body waves. Instead, we estimated the effect of topography on the dispersion measurements for two extreme cases, as similar tests have been previously performed (Jaxybulatov *et al.* 2014; Benediktsdóttir *et al.* 2017; Jeddi *et al.* 2017). We estimated differences in the dispersion velocity for the station-pair with the longest interstation distance (65 km) and a large elevational gradient (1.9 km, stations SS02 and TP01), as well as for the pair with the highest altitude difference (~1 km) to the interstation distance (17 km) (stations SS04 and JJU, Fig. 1). Simple calculations assuming rays propagating along the surface without accounting for frequency effects showed that the possible velocity uncertainties due to topography were 0.2 and 0.7 per cent for the former and latter pairs, respectively (Jaxybulatov *et al.* 2014; Benediktsdóttir

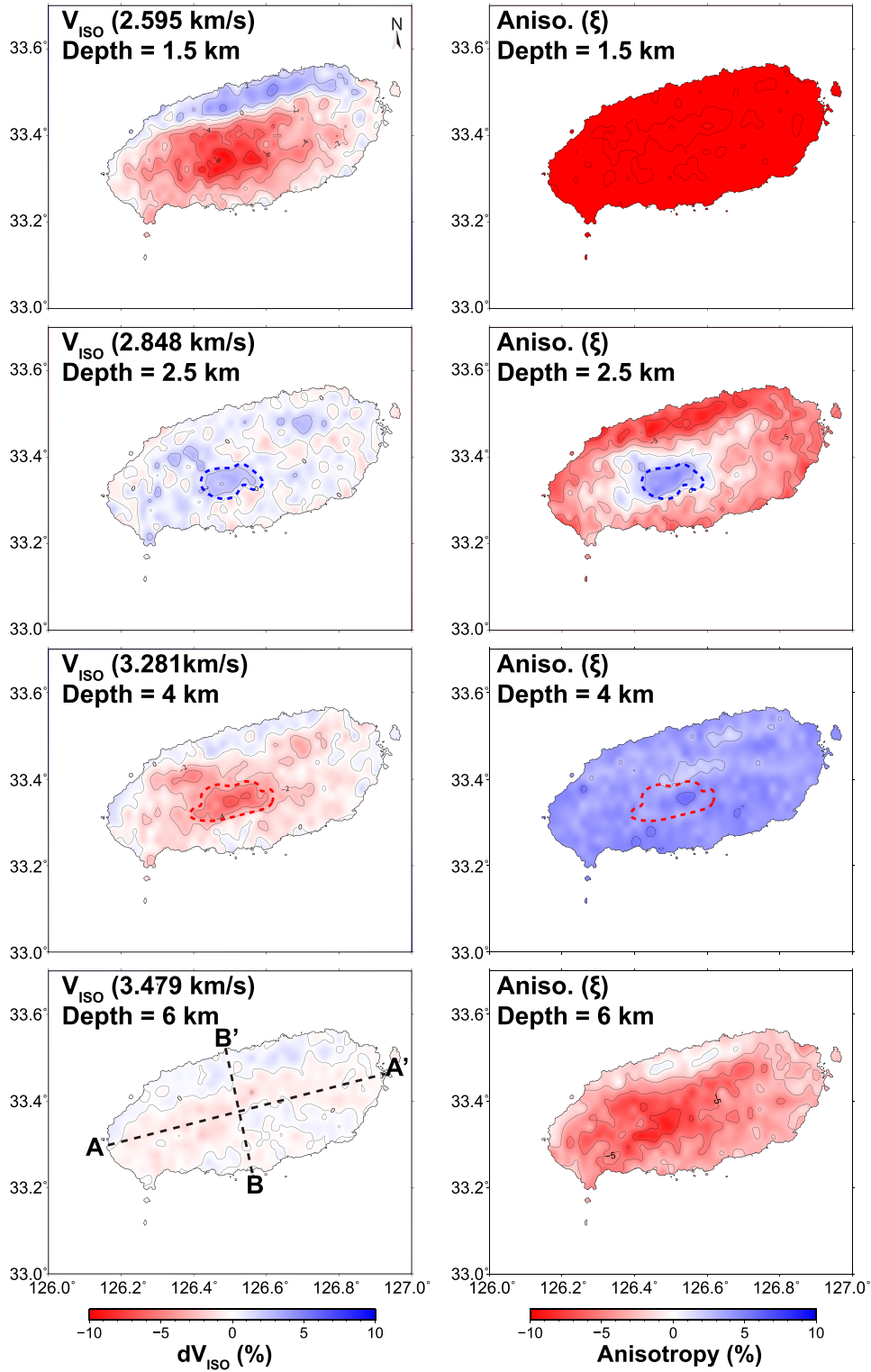


Figure 10. Horizontal slices of the 3-D V_{ISO} models and anisotropic models at depths of 1–6 km. Relative V_{ISO} was calculated based on the average of the V_{ISO} models for grids following the coastline. Blue and red dashed contour lines show the second and third layers, as categorized from the patterns in the V_{ISO} and ξ models. Black dashed lines represent transects of vertical sections in Fig. 11.

et al. 2017; Jeddi et al. 2017). These uncertainties are insignificant considering the velocity perturbations in the dispersion maps (Figs 4 and 5) and variances in data, which were $\sim 15\text{--}20$ per cent of the mean dispersion curves (Fig. 3). In particular, much larger

variations in velocity (>5 per cent), compared to the estimated uncertainties, were consistently estimated in all of the shortest period maps (2-s maps in Figs 4 and 5), which are the most sensitive periods to topographical variation.

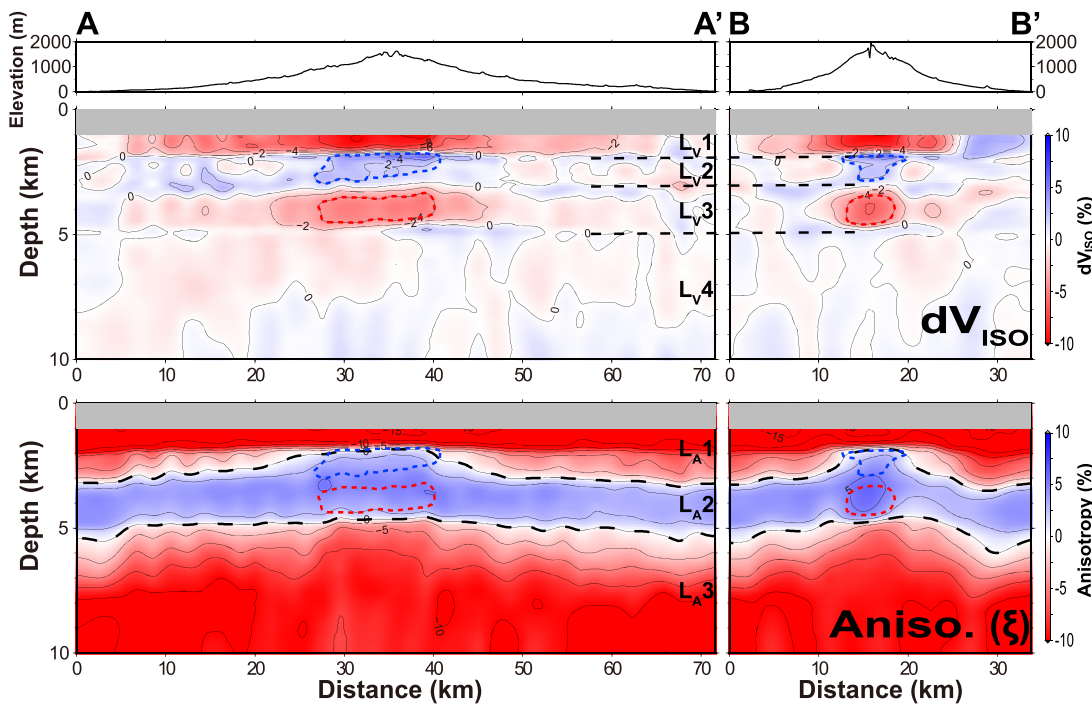


Figure 11. Vertical sections of the $V_{\text{ISO}} = (2V_{\text{SV}} + V_{\text{SH}})/3$ and anisotropy models following the A–A' and B–B' transects shown in Fig. 10.

As a way to verify our inversion results with strong radial anisotropy (Fig. 8), we conducted a recovery test using synthetically generated data. To calculate synthetic RGV, RPV, LGV and LPV dispersion curves, we used V_{ISO} and ξ models at the top of Mt Halla (Fig. 8) and simplified them to have three layers over a half-space (Fig. 12). Notably, the third layer exhibited abruptly large and positive radial anisotropy (10 per cent) from the dominantly negative background of radial anisotropy (Fig. 12). Residual errors between the observed and modeled data in Fig. 8 were applied as data error to the calculated synthetic dispersion curves. The inversion results from the synthetic data showed that the input anomalies were well recovered in both isotropic and radial anisotropic models (Fig. 12).

The shallowest layer (<2 km) had relatively slow isotropic structures with vertically fast anisotropy ($L_{\text{V}1}$ and $L_{\text{A}1}$ in Fig. 11) at the central and southern part of JI (Fig. 10). The surface geology and data from a drilling survey indicate that JI has generally thick sedimentary structures (~ 2 km), which have mainly been formed by hydrovolcanic eruptions and pyroclastic depositions (Koh *et al.* 2013; Yoon *et al.* 2014). In general, such horizontal layering of deposited materials results in positive radial anisotropy due to both CPOs and SPOs, as reported in several previous studies (Shapiro *et al.* 2004; Meissner *et al.* 2006; Ko & Jung 2015; Almqvist & Mainprice 2017; Jung 2017). Massive lava flows along a gentle slope also cause positive anisotropy (e.g. Mordret *et al.* 2015). The observations on JI are inconsistent with the surface features. Similar negative anisotropy has been reported in volcanoes dominated by vertically aligned SPOs (e.g. Spica *et al.* 2017; Lynner *et al.* 2018). Spica *et al.* (2017) showed that negative radial anisotropy was dominant within a low-velocity layer at the central part of the Colima volcano, with a dyke swarm above a shallow magma chamber. Vertically developed crustal magma plumbing systems have also been detected with negative anisotropy (Lynner *et al.* 2018).

It has been known that JI and the volcanic bodies in it were formed by the overlap of more than 400 scattered small cones from laterally distributed magma plumbing structures (Park *et al.* 2008; Shin *et al.* 2012; Koh *et al.* 2013; Brenna *et al.* 2015; Song *et al.* 2018). Our observations from the top layer correspond to previous results that suggested that a vertically aligned SPO, due to highly developed dyke swarms (Fig. 13) over most of JI, could play a major role in producing the negatively anisotropic structures, which are similar to many other regions worldwide (Jaxybulatov *et al.* 2014; Tibaldi 2015; Spica *et al.* 2017; Çakır 2018; Lynner *et al.* 2018). Volcanic activities forming the central vent (Mt Halla) were episodic within limited time periods during the continuous and small-scaled monogenetic volcanism via ubiquitous cones (Brenna *et al.* 2012, 2015; Koh *et al.* 2013; Yoon *et al.* 2014). Therefore, the formation of the shallow volcano-sedimentary structures may have been less affected by the central eruptions, but rather by the more heterogeneous deposition filling in gaps between cones, which resulted in weaker horizontally fast anisotropy than distributed and vertically aligned structures (i.e. dyke swarms).

In the second and third layers (2–5 km), the pattern of radial anisotropy changed from negative to strongly positive (greater than ~ 5 per cent, Fig. 10 and $L_{\text{A}2}$ in Fig. 11). At upper crustal depths, the alignment of fluid-saturated microfissures (i.e. SPO) is the primary origin of anisotropy (Okaya *et al.* 1995). To produce positive radial anisotropy, the presence of laterally elongated cracks is necessary, along with an alignment of regional tectonic stress fields (e.g. Guo *et al.* 2012). Specifically, in volcanic fields, such structures could be formed by cooled and fluid-filled melt lenses, sills or layered magma stores (Shapiro *et al.* 2004; Meissner *et al.* 2006; Jaxybulatov *et al.* 2014; Spica *et al.* 2017; Jiang *et al.* 2018; Lynner *et al.* 2018). The formation of these volcanic structures has been commonly understood as resulting from changes in vertical volume (e.g. caldera collapse, Masterlark *et al.* 2010; Cashman & Giordano 2014; Jaxybulatov *et al.* 2014; Ward *et al.* 2014; Benediktsdóttir

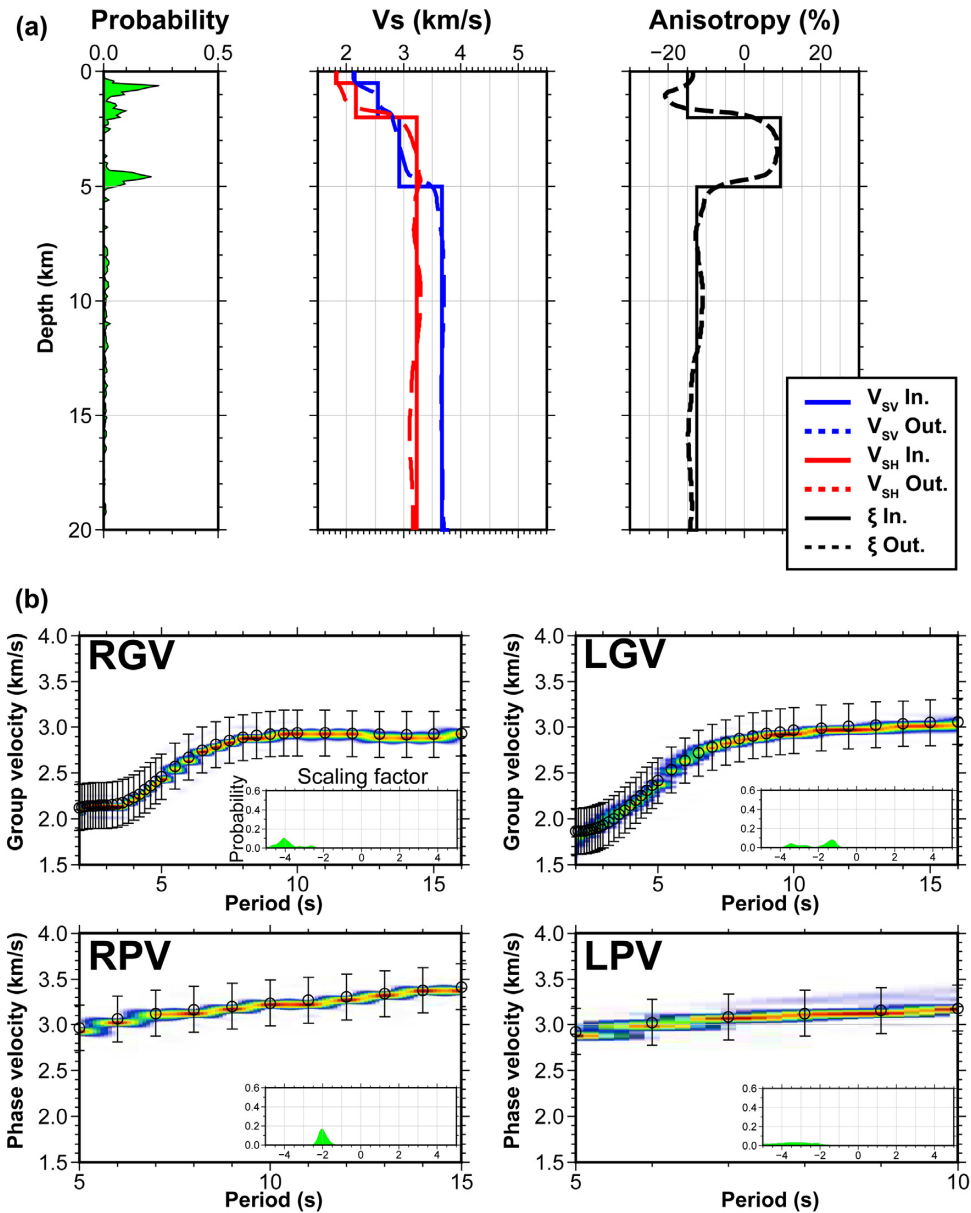


Figure 12. (a) Synthetic results of 1-D shear velocity and anisotropy models. Rayleigh and Love dispersion curves were calculated using input V_{SV} , V_{SH} and anisotropy models (red, blue and black solid lines, respectively) similar to those observed in the centre of Mt Halla. The V_{SV} , V_{SH} and radial anisotropy models were inverted following our inversion scheme. (b) Posterior distributions of predicted synthetic data with the observed data.

et al. 2017; Jedd et al. 2017). More generally, recent studies have shown that the horizontal magma transportation at shallow depths in volcanic fields is strongly controlled by the applied stress related to topographic loading, faults and heterogeneities in local stress fields (Ishizuka et al. 2008; Tibaldi et al., 2015; González et al. 2013).

Horizontally elongated magma structures at upper crustal depths have been reported in various volcanic regions (Ishizuka et al. 2008; Spica et al. 2017; Çakır 2018; Lynner et al. 2018). All of these regions have shown highly similar patterns to the anisotropic structure in this study, with embedded and horizontally layered magma structures at a middle depth between the vertically aligned structures above and below. Ishizuka et al. (2008) reported structures of laterally transported magma over 30 km at 5 km depth below the Hachijo Nishiyama volcano. They explained that the structure was formed by vertical pressures from the loading of the overlying rock

mass and the upward pushing of magma from bottom plumbing structures. Çakır (2018) imaged a similar scale positive anisotropy (>10 per cent) at shallow crustal depths beneath the Aegean region within negative radially anisotropic ambient structures. They specified the lateral structure as a sill (or small-scale horizontally elongated magma chamber) complex in a predominantly extensional tectonic setting. In extensional regimes, similar sill intrusions are developed at deeper depths (Spica et al. 2017; Lynner et al. 2018).

It has been suggested that volcanism was less focused on the central vent, and thus no large caldera formed on JI (Brenna et al. 2012, 2015). The primary stress regime (Shin et al. 2012) was extensional during the period of JI volcanism, which occurred in a backarc setting due to the subduction of the Philippine Sea Plate (Brenna et al. 2015; Kim et al. 2016). Together with the striking similarity in the

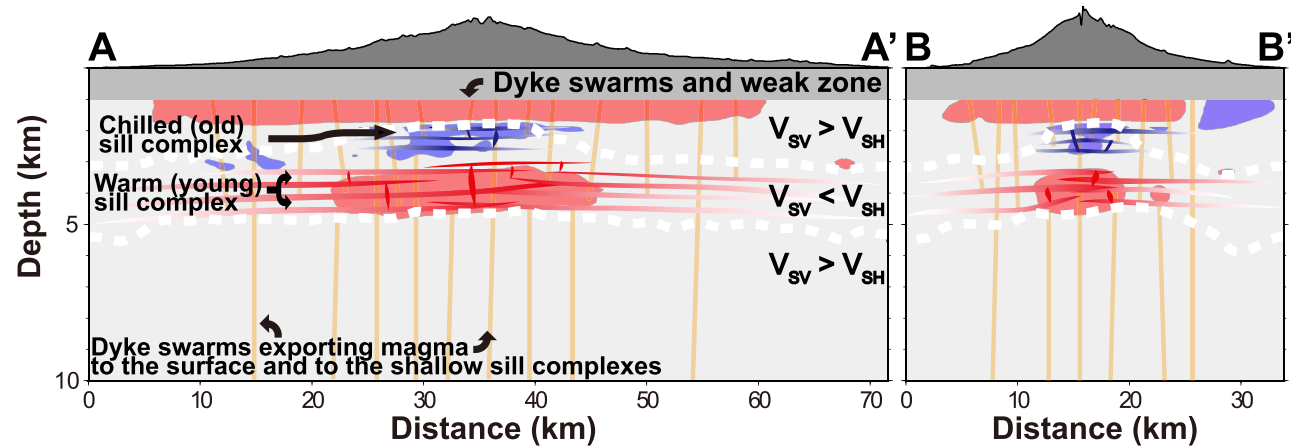


Figure 13. Model of the magma plumbing system of JI. Blue and red shaded zones with gray dashed lines represent the ± 2 per cent isosurfaces of the relative isotopic model, and white dashed lines show the boundaries of anisotropic changes.

patterns of layered horizontally and vertically aligned magma structures beneath different volcanoes, the features of magma structures below JI indicate that the layer with positive radial anisotropy at a depth of 2–5 km likely consists of intrusive sills fed by scattered cones and the central volcano.

Overlapping with the isotropic velocity distribution, the horizontally fast anisotropic structure at the middle depth of 2–5 km was divided into two parts, with faster and slower isotropic velocities (the second and third layer, respectively) below the central volcano and over a limited volume of 600 km^3 (L_{V2} and L_{V3} in Fig. 11). The perturbation of shear waves can be caused by many factors, including thermal variations, a compositional dichotomy and the existence of fluids or melts (Artemieva *et al.* 2004; Dalton *et al.* 2009; Cammarano *et al.* 2011). Separation and focusing of crustal fluids is less likely to occur in a limited part of highly developed sill complexes. Additionally, the relatively small reduction in velocity (up to –4 per cent) and lack of current volcanism at the surface rule out the existence of melted materials.

Compositional variation might be caused by magma separation within a magma structure via fractional crystallization, resulting in the faster, more mafic upper layer overlying the slower felsic layer (Shervais *et al.* 2006; Ishizuka *et al.* 2008). However, in the case of JI, it is difficult to explain the upward deposition of crystallized mafic materials and the consistent horizontally fast direction of both sides with different compositions. Therefore, it is more reasonable to interpret these structures in terms of thermal variations. Differences in cooling time present a plausible explanation for the temperature variation in the same sill texture. In the case of simultaneous injections of magma and the formation of a sill structure, cooling speeds will change with depth, which could control the variation in velocity. However, the sharp transition in isotropic velocity is more favourable to a time lag between the formation of the upper and lower layers. The second layer may have been formed first, before the third layer, in the same setting that produced similar sill structures. Many similar structures have been reported in volcanic systems with multiple layers of sill-like magma accumulations in the shallow crust (e.g. Cervelli & Miklius 2003; Peltier *et al.* 2009; Chadwick *et al.* 2011; Bagnardi & Amelung 2012; Baker & Amelung 2012).

Regional horizons of neutral buoyancy, magma supply rates and thermomechanical structure in the crust control the depth distribution of multiple small magma chambers (Clague & Dixon 2000;

Hildner *et al.* 2012; González *et al.* 2013; Edmonds *et al.* 2019). Based on the magma supply rate on JI ($\sim 0.0003 \text{ km}^3 \text{ yr}^{-1}$), volcanoes on Réunion and in the Galápagos are particularly similar to JI, with extensive distributions of sill-like chambers at 2–7 km depths (Edmonds *et al.* 2019). Though there is no clear evidence of focusing for volcanic activities on the central volcano, the contrast in the thickness of the laterally fast anisotropic layer between this area and the surrounding regions shows that magma supplies to the central volcano lasted longer. While speculative, the formation of the third layer by sill intrusions could have pushed up the second layer, building a high-topography central volcano (Archer *et al.* 2005; McLean *et al.* 2017). Compared to the surrounding small monogenic cones, this would correspond to episodic eruptions with larger volumes of magma (Brenna *et al.* 2012, 2015; Koh *et al.* 2013; Yoon *et al.* 2014).

Song *et al.* (2018) showed that magma on JI originated from the sublithospheric upper mantle interacting intensely with the lithosphere to form broadly distributed magma structures in the deeper crust. The basement, with its negative radial anisotropy, is explained as the magma plumbing system connecting from the deep source to the structures in the shallow crust (L_{V4} and L_{A3} in Fig. 11). A setting within the deeper crustal dyke structures and shallow sill layers of diverse scales has often been reported in many volcanoes (e.g. Mordret *et al.* 2015; Tibaldi 2015; Godfrey *et al.* 2017; Spica *et al.* 2017; Çakır 2018; Lynner *et al.* 2018). Depending upon the flux of magma and the level of ambient stress, this type of vertical plumbing system consists of a few large dykes or many smaller but more widely distributed dyke systems. Together with the monogenic and randomly distributed eruptions over time and space, the more homogeneous and vertically fast anisotropy indicates the latter structure is more plausible (Brenna *et al.* 2012, 2015; Yoon *et al.* 2014; Mordret *et al.* 2015; Godfrey *et al.* 2017; Spica *et al.* 2017; Çakır 2018; Lynner *et al.* 2018).

6 CONCLUSIONS

In this study, we constructed 3-D V_{ISO} and ξ models of JI, an isolated intraplate volcano located offshore of the southeastern Korean Peninsula, by applying hierarchical and transdimensional Bayesian inversions with temporary seismic network data. The 3-D V_{ISO} and ξ models of JI show that various types of plumbing systems exist in the upper crust. A top layer that extends down to 2 km with slow

V_{ISO} and strongly negative ξ (L_V1 and L_A1) could represent vertically aligned SPOs due to the highly developed dyke swarms related to the scattered small cones over most of JI. The second and third layers with positive ξ (L_A2) may be interpreted as multiple layers of sill-like magma accumulation in the shallow crust, while there is central thermal variation between the two layers (L_V2 and L_V3) due to episodic eruptions with larger volumes of magma and differences in cooling time. Moving away from the centre of JI, these central velocity anomalies decrease and the structure with first positive ξ values becomes thinner. The vertically fast basement (ξ , L_A3), with generally neutral V_{ISO} and where average upper-middle crustal velocities are slower than those of the southern Korean Peninsula, over the entire JI (L_V4) is explained as the magma plumbing system connecting from the deep source reported from the results of a previous teleseismic tomography study that used body wave data on JI. These characteristic plumbing systems have supplied various types of magma from deeper sources and have been involved in complex and episodic eruptions, which ultimately formed JI.

ACKNOWLEDGEMENTS

The authors would like to thank Jeong-Ung Woo, Sungwon Cho and Juhwan Kim of Seoul National University and Jechan Park, Hyun Ho Jang, Minook Kim, ChangHwan Kong, Euna Park, Hyejin Park and Dabeen Heo of Pukyong National University for their assistance in the field deployment of the temporary seismic network. We also thank Gee-Pyo Kim (Jeju Special Self-Governing Province), Soo-Hyoung Lee and Kyoochul Ha (KIGAM) for making the said deployment possible. Data were partly acquired from the KMA and KIGAM. Most of the figures were generated using Generic Mapping Tools (Wessel *et al.*, 2013). This work was funded by the Korea Meteorological Administration Research and Development Program under Grant KMI 2018–02910. A temporary seismic network data in this study is not opened.

REFERENCES

- Aloisi, M., Cocina, O., Neri, G., Orecchio, B. & Privitera, E., 2002. Seismic tomography of the crust underneath the Etna volcano, Sicily, *Phys. Earth planet. Inter.*, **134**(3–4), 139–155.
- Almqvist, B.S. & Mainprice, D., 2017. Seismic properties and anisotropy of the continental crust: predictions based on mineral texture and rock microstructure. *Rev. Geophys.*, **55**(2), 367–433.
- Archer, S.G., Bergman, S.C., Iliffe, J., Murphy, C.M. & Thornton, M., 2005. Palaeogene igneous rocks reveal new insights into the geodynamic evolution and petroleum potential of the Rockall Trough, NE Atlantic Margin, *Basin Res.*, **17**(1), 171–201.
- Artemieva, I.M., Billien, M., Lévéque, J.J. & Mooney, W.D., 2004. Shear wave velocity, seismic attenuation, and thermal structure of the continental upper mantle, *Geophys. J. Int.*, **157**(2), 607–628.
- Bagnardi, M. & Amelung, F., 2012. Space-geodetic evidence for multiple magma reservoirs and subvolcanic lateral intrusions at Fernandina Volcano, Galápagos Islands, *J. geophys. Res. Solid Earth*, **117**(B10), doi:10.1029/2012JB009465.
- Baker, S. & Amelung, F., 2012. Top-down inflation and deflation at the summit of Kīlauea Volcano, Hawai‘i observed with InSAR, *J. geophys. Res.*, **117**(B12), doi:10.1029/2011JB009123.
- Benediktsdóttir, Á., Gudmundsson, Ó., Brandsdóttir, B. & Tryggvason, A., 2017. Ambient noise tomography of Eyjafjallajökull volcano, Iceland, *J. Volc. Geotherm. Res.*, **347**, 250–263.
- Bensen, G.D., Ritzwoller, M.H., Barnin, M.P., Levshin, A.L., Lin, F., Moschetti, M.P. & Yang, Y., 2007. Processing seismic ambient noise data to obtain reliable broad-band surface wave dispersion measurements, *Geophys. J. Int.*, **169**(3), 1239–1260.
- Bodin, T., Leiva, J., Romanowicz, B., Maupin, V. & Yuan, H., 2016. Imaging anisotropic layering with Bayesian inversion of multiple data types, *Geophys. J. Int.*, **206**(1), 605–629.
- Brenna, M., Cronin, S.J., Smith, I.E., Maas, R. & Sohn, Y.K., 2012. How small-volume basaltic magmatic systems develop: a case study from the Jeju Island Volcanic Field, Korea. *J. Petrol.*, **53**(5), 985–1018.
- Brenna, M., Cronin, S.J., Keresztsuri, G., Sohn, Y.K., Smith, I.E. & Wijsbrans, J., 2015. Intraplate volcanism influenced by distal subduction tectonics at Jeju Island, Republic of Korea, *Bull. Volcanol.*, **77**(1), 7, doi:10.1007/s00445-014-0896-5.
- Brenguier, F., Shapiro, N.M., Campillo, M., Nercissian, A. & Ferrazzini, V., 2007. 3-D surface wave tomography of the Piton de la Fournaise volcano using seismic noise correlations, *Geophys. Res. Lett.*, **34**(2), doi:10.1029/2006GL028586.
- Cakir, Ö., 2018. Seismic crust structure beneath the Aegean region in southwest Turkey from radial anisotropic inversion of Rayleigh and Love surface waves, *Acta Geophys.*, **66**(6), 1303–1340.
- Cammarano, F., Tackley, P. & Boschi, L., 2011. Seismic, petrological and geodynamical constraints on thermal and compositional structure of the upper mantle: global thermochemical models, *Geophys. J. Int.*, **187**(3), 1301–1318.
- Cashman, K.V. & Giordano, G., 2014. Calderas and magma reservoirs, *J. Volc. Geotherm. Res.*, **288**, 28–45.
- Chadwick, W.W., Jónsson, S., Geist, D.J., Poland, M., Johnson, D.J., Batt, S. & Ruiz, A., 2011. The May 2005 eruption of Fernandina volcano, Galápagos: the first circumferential dike intrusion observed by GPS and InSAR, *Bull. Volcanol.*, **73**(6), 679–697.
- Cervelli, P.F. & Miklius, A., 2003. The shallow magmatic system of Kilauea Volcano, *US Geol. Surv. Prof. Pap.*, **1676**, 149–163.
- Choi, S.H., Jwa, Y.J. & Lee, H.Y., 2001. Geothermal gradient of the upper mantle beneath Jeju Island, Korea: evidence from mantle xenoliths, *Island Arc*, **10**(2), 175–193.
- Clague, D.A. & Dixon, J.E., 2000. Extrinsic controls on the evolution of Hawaiian ocean island volcanoes, *Geochem. Geophys. Geosyst.*, **1**(4), 1–9.
- Crampin, S., 1981. A review of wave motion in anisotropic and cracked elastic-media, *Wave Motion*, **3**(4), 343–391.
- Crampin, S., 1984. An introduction to wave propagation in anisotropic media, *Geophys. J. Int.*, **76**(1), 17–28.
- Crampin, S., 1989. Suggestions for a consistent terminology for seismic anisotropy 1, *Geophys. Prospect.*, **37**(7), 753–770.
- Crampin, S. & Lovell, J.H., 1991. A decade of shear-wave splitting in the Earth's crust: what does it mean? What use can we make of it? and what should we do next? *Geophys. J. Int.*, **107**(3), 387–407.
- Dalton, C.A., Ekström, G. & Dziewonski, A.M., 2009. Global seismological shear velocity and attenuation: a comparison with experimental observations, *Earth planet. Sci. Lett.*, **284**(1–2), 65–75.
- Edmonds, M., Cashman, K.V., Holness, M. & Jackson, M., 2019. Architecture and dynamics of magma reservoirs, *Phil. Trans. R. Soc. Lond. A*, **377**, 20180298, doi:10.1098/rsta.2018.0298.
- Eilon, Z., Abers, G.A., Jin, G. & Gaherty, J.B., 2014. Anisotropy beneath a highly extended continental rift, *Geochem. Geophys. Geosyst.*, **15**(3), 545–564.
- González, P.J., Samsonov, S.V., Pepe, S., Tiampo, K.F., Tizzani, P., Casu, F. & Sansosti, E., 2013. Magma storage and migration associated with the 2011–2012 El Hierro eruption: implications for crustal magmatic systems at oceanic island volcanoes, *J. geophys. Res.*, **118**(8), 4361–4377.
- Godfrey, H.J., Fry, B. & Savage, M.K., 2017. Shear-wave velocity structure of the Tongariro volcanic centre, New Zealand: fast Rayleigh and slow Love waves indicate strong shallow anisotropy, *J. Volc. Geotherm. Res.*, **336**, 33–50.
- Guo, Z., Gao, X., Wang, W. & Yao, Z., 2012. Upper-and mid-crustal radial anisotropy beneath the central Himalaya and southern Tibet from seismic ambient noise tomography, *Geophys. J. Int.*, **189**(2), 1169–1182.
- Guo, Z., Yang, Y. & Chen, Y.J., 2016. Crustal radial anisotropy in Northeast China and its implications for the regional tectonic extension, *Geophys. J. Int.*, **207**(1), 197–208.

- Herrmann, R.B. & Ammon, C.J., 2002. *Computer Programs In Seismology: Surface Waves, Receiver Functions and Crustal Structure. Version 3.30*, Saint Louis University.
- Hildner, E., Klügel, A. & Hansteen, T.H., 2012. Barometry of lavas from the 1951 eruption of Fogo, Cape Verde Islands: implications for historic and prehistoric magma plumbing systems, *J. Volc. Geotherm. Res.*, **217**, 73–90.
- Huang, H., Yao, H. & van der Hilst, R.D., 2010. Radial anisotropy in the crust of SE Tibet and SW China from ambient noise interferometry, *Geophys. Res. Lett.*, **37**(21), doi:10.1029/2010GL044981.
- Huang, H.H., Lin, F.C., Schmandt, B., Farrell, J., Smith, R.B. & Tsai, V.C., 2015. The Yellowstone magmatic system from the mantle plume to the upper crust, *Science*, **348**(6236), 773–776.
- Ishizuka, O., Geshi, N., Itoh, J.I., Kawanabe, Y. & TuZino, T., 2008. The magmatic plumbing of the submarine Hachijo NW volcanic chain, Hachijojima, Japan: long-distance magma transport? *J. geophys. Res.*, **113**(B8), doi:10.1029/2007JB005325.
- Jaxybulatov, K., Shapiro, N.M., Koulakov, I., Mordret, A., Landès, M. & Sens-Schönfelder, C., 2014. A large magmatic sill complex beneath the Toba Caldera, *Science*, **346**(6209), 617–619.
- Jeddi, Z., Gudmundsson, O. & Tryggvason, A., 2017. Ambient-noise tomography of Katla Volcano, South Iceland, *J. Volc. Geotherm. Res.*, **347**, 264–277.
- Jeon, T., Kim, K.Y. & Woo, N., 2013. S-wave velocities beneath Jeju Island, Korea, using inversion of receiver functions and the H- κ stacking method, *Geophys. Geophys. Explor.*, **16**(1), 18–26.
- Jiang, C., Schmandt, B., Farrell, J., Lin, F.C. & Ward, K.M., 2018. Seismically anisotropic magma reservoirs underlying silicic calderas, *Geology*, **46**(8), 727–730.
- Jung, H., 2017. Crystal preferred orientations of olivine, orthopyroxene, serpentine, chlorite, and amphibole, and implications for seismic anisotropy in subduction zones: a review, *Geosci. J.*, **21**(6), 985–1011.
- Kennett, B.L.N., Sambridge, M.S. & Williamson, P.R., 1988. Subspace methods for large inverse problems with multiple parameter classes, *Geophys. J. Int.*, **94**(2), 237–247.
- Kim, J. & Jung, H., 2019. New crystal preferred orientation of amphibole experimentally found in simple shear, *Geophys. Res. Lett.*, **46**(22), 12 996–13 005.
- Kim, J.I., Choi, S.H., Koh, G.W., Park, J.B. & Ryu, J.S., 2019. Petrogenesis and mantle source characteristics of volcanic rocks on Jeju Island, South Korea, *Lithos*, **326**, 476–490.
- Kim, K.Y. & Hong, M.H., 2012. Shear-wave velocity structure of Jeju Island, Korea, *Geosci. J.*, **16**(1), 35–45.
- Kim, S., Rhie, J. & Kim, G., 2011. Forward waveform modelling procedure for 1-D crustal velocity structure and its application to the southern Korean Peninsula, *Geophys. J. Int.*, **185**(1), 453–468.
- Kim, S., Tkalcic, H., Rhie, J. & Chen, Y., 2016. Intraplate volcanism controlled by back-arc and continental structures in NE Asia inferred from transdimensional Bayesian ambient noise tomography, *Geophys. Res. Lett.*, **43**, 8390–8398.
- Kim, S., Tkalcic, H. & Rhie, J., 2017. Seismic constraints on magma evolution beneath Mount Baekdu (Changbai) volcano from transdimensional Bayesian inversion of ambient noise data, *J. geophys. Res.*, **122**, 5452–5473.
- Ko, B. & Jung , H., 2015. Crystal preferred orientation of an amphibole experimentally deformed by simple shear, *Nature communications*, **6**, 1, 1–10, 10.1038/ncomms7586, 2041–1723.
- Koh, G.W., Park, J.B., Kang, B.R., Kim, G.P. & Moon, D.C., 2013. Volcanism in Jeju Island, *J. Geol. Soc. Korea*, **49**(2), 209–230.
- Klügel, A., Hansteen, T.H. & Galipp, K., 2005. Magma storage and underplating beneath Cumbre Vieja volcano, la Palma (Canary Islands), *Earth planet. Sci. Lett.*, **236**(1–2), 211–226.
- Leary, P.C., Crampin, S. & McEvilly, T.V., 1990. Seismic fracture anisotropy in the Earth's crust: an overview, *J. geophys. Res.*, **95**(B7), 11 105–11 114.
- Li, Z., Ni, S., Zhang, B., Bao, F., Zhang, S., Deng, Y. & Yuen, D.A., 2016. Shallow magma chamber under the Wudalianchi volcanic field unveiled by seismic imaging with dense array, *Geophys. Res. Lett.*, **43**(10), 4954–4961.
- Lin, F.C., Moschetti, M.P. & Ritzwoller, M.H., 2008. Surface wave tomography of the western United States from ambient seismic noise: Rayleigh and Love wave phase velocity maps, *Geophys. J. Int.*, **173**(1), 281–298.
- Lynner, C., Beck, S.L., Zandt, G., Porritt, R.W., Lin, F.C. & Eilon, Z.C., 2018. Midcrustal deformation in the Central Andes constrained by radial anisotropy, *J. geophys. Res.*, **123**(6), 4798–4813.
- Mainprice, D. & Nicolas, A., 1989. Development of shape and lattice preferred orientations: application to the seismic anisotropy of the lower crust, *J. Struct. Geol.*, **11**(1–2), 175–189.
- Masterlark, T., Haney, M., Dickinson, H., Fournier, T. & Searcy, C., 2010. Rheologic and structural controls on the deformation of Okmok volcano, Alaska: FEMs, InSAR, and ambient noise tomography, *J. geophys. Res.*, **115**(B2), doi:10.1029/2009JB006324.
- McLean, C.E., Schofield, N., Brown, D.J., Jolley, D.W. & Reid, A., 2017. 3D seismic imaging of the shallow plumbing system beneath the Ben Nevis monogenetic volcanic field: Faroe–Shetland Basin, *J. Geol. Soc.*, **174**(3), 468–485.
- Meissner, R., Rabbel, W. & Kern, H., 2006. Seismic lamination and anisotropy of the lower continental crust, *Tectonophysics*, **416**(1–4), 81–99.
- Mordret, A., Rivet, D., Landès, M. & Shapiro, N.M., 2015. Three-dimensional shear velocity anisotropic model of Piton de la Fournaise Volcano (La Réunion Island) from ambient seismic noise, *J. geophys. Res.*, **120**(1), 406–427.
- Moschetti, M.P., Ritzwoller, M.H., Lin, F.C. & Yang, Y., 2010. Crustal shear wave velocity structure of the western United States inferred from ambient seismic noise and earthquake data, *J. geophys. Res.*, **115**(B10), doi:10.1029/2010JB007448.
- Nakamura, E., McCulloch, M.T. & Campbell, I.H., 1990. Chemical geodynamics in the back-arc region of Japan based on the trace element and Sr-Nd isotopic compositions, *Tectonophysics*, **174**(3–4), 207–233.
- Okaya, D., Christensen, N., Stanley, D., Stern, T. & Transect, S.I.G., 1995. Crustal anisotropy in the vicinity of the Alpine Fault zone, South Island, New Zealand, *New Zeal. J. Geol. Geophys.*, **38**(4), 579–583.
- Park, K.H., Koh, D.C., Kim, Y.C., Moon, S.H., Seong, K.S., Shin, J.H. & Kim, G.Y., 2008. Integrated analysis of groundwater occurrence, Jeju, Korea Institute of Geoscience and Mineral Resources, GP2007-009-04-2008(2), pp. 365 (in Korean with English abstract).
- Paulatto, M., Minshull, T.A., Baptie, B., Dean, S., Hammond, J.O., Henstock, T. & Ryan, G., 2010. Upper crustal structure of an active volcano from refraction/reflection tomography, Montserrat, Lesser Antilles, *Geophys. J. Int.*, **180**(2), 685–696.
- Peltier, A., Staudacher, T., Bacheler, P. & Cayol, V., 2009. Formation of the April 2007 caldera collapse at Piton de La Fournaise volcano: Insights from GPS data, *J. Volc. Geotherm. Res.*, **184**(1–2), 152–163.
- Rawlinson, N. & Sambridge, M., 2005. The fast marching method: an effective tool for tomographic imaging and tracking multiple phases in complex layered media, *Explor. Geophys.*, **36**(4), 341–350.
- Russell, J.B., Gaherty, J.B., Lin, P.Y.P., Lizarralde, D., Collins, J.A., Hirth, G. & Evans, R.L., 2019. High-resolution constraints on Pacific upper mantle petrofabric inferred from surface-wave anisotropy, *J. geophys. Res.*, **124**(1), 631–657.
- Shapiro, N.M., Ritzwoller, M.H., Molnar, P. & Levin, V., 2004. Thinning and flow of Tibetan crust constrained by seismic anisotropy, *Science*, **305**(5681), 233–236.
- Shervais, J.W., Vetter, S.K. & Hanan, B.B., 2006. Layered mafic sill complex beneath the eastern Snake River Plain: evidence from cyclic geochemical variations in basalt, *Geology*, **34**(5), 365–368.
- Shin, Y.H., Choi, K.S., Koh, J.S., Yun, S.H., Nakamura, E. & Na, S.H., 2012. Lithospheric-folding-based understanding on the origin of the back-arc basaltic magmatism beneath Jeju volcanic island, *Tectonics*, **31**(4), doi:10.1029/2011TC003092.
- Song, L.P., Koch, M., Koch, K. & Schlittenhardt, J., 2004. 2-D anisotropic Pn-velocity tomography underneath Germany using regional traveltimes, *Geophys. J. Int.*, **157**(2), 645–663.
- Song, J.H., Kim, S., Rhie, J., Lee, S.H., Kim, Y. & Kang, T.S., 2018. Imaging of lithospheric structure beneath Jeju Volcanic Island by teleseismic traveltome tomography, *J. geophys. Res.*, **123**(8), 6784–6801.

- Spica, Z., Legrand, D., Iglesias, A., Walter, T.R., Heimann, S., Dahm, T. & Pardo, M., 2015. Hydrothermal and magmatic reservoirs at Lazufre volcanic area, revealed by a high-resolution seismic noise tomography, *Earth planet. Sci. Lett.*, **421**, 27–38.
- Spica, Z., Perton, M. & Legrand, D., 2017. Anatomy of the Colima volcano magmatic system, Mexico, *Earth planet. Sci. Lett.*, **459**, 1–13.
- Stankiewicz, J., Ryberg, T., Haberland, C. & Natawidjaja, D., 2010. Lake Toba volcano magma chamber imaged by ambient seismic noise tomography, *Geophys. Res. Lett.*, **37**(17), doi:10.1029/2010GL044211.
- Tatsumi, Y., Shukuno, H., Yoshikawa, M., Chang, Q., Sato, K. & Lee, M.W., 2004. The petrology and geochemistry of volcanic rocks on Jeju Island: Plume magmatism along the Asian continental margin, *J. Petrol.*, **46**(3), 523–553.
- Tibaldi, A., 2015. Structure of volcano plumbing systems: a review of multi-parametric effects, *J. Volc. Geotherm. Res.*, **298**, 85–135.
- Tomar, G., Shapiro, N.M., Mordret, A., Singh, S.C. & Montagner, J.P., 2017. Radial anisotropy in Valhall: ambient noise-based studies of Scholte and Love waves. *Geophys. J. Int.*, **208**(3), 1524–1539.
- Ward, K.M., Zandt, G., Beck, S.L., Christensen, D.H. & McFarlin, H., 2014. Seismic imaging of the magmatic underpinnings beneath the Altiplano–Puna volcanic complex from the joint inversion of surface wave dispersion and receiver functions, *Earth planet. Sci. Lett.*, **404**, 43–53.
- Xie, J., Ritzwoller, M.H., Shen, W., Yang, Y., Zheng, Y. & Zhou, L., 2013. Crustal radial anisotropy across eastern Tibet and the western Yangtze craton. *J. geophys. Res.*, **118**(8), 4226–4252.
- Yao, H., van Der Hilst, R.D. & Maarten, V., 2006. Surface-wave array tomography in SE Tibet from ambient seismic noise and two-station analysis—I. Phase velocity maps, *Geophys. J. Int.*, **166**(2), 732–744.
- Yoon, S., Jung, C.Y., Hyun, W.H. & Song, S.T., 2014. Tectonic history of Jeju Island, *J. Geol. Soc. Korea*, **50**(4), 457–474.
- Zheng, Y., Shen, W., Zhou, L., Yang, Y., Xie, Z. & Ritzwoller, M.H., 2011. Crust and uppermost mantle beneath the North China Craton, northeastern China, and the Sea of Japan from ambient noise tomography, *J. geophys. Res.*, **116**(B12), doi:10.1029/2011JB008637.